Mechanisms of Auger-induced chemistry derived from wave packet dynamics

Julius T. Su and William A. Goddard III[1]

Materials and Process Simulation Center, California Institute of Technology, Pasadena, CA 91125

Contributed by William A. Goddard III, December 1, 2008 (sent for review September 19, 2008)

To understand how core ionization and subsequent Auger decay lead to bond breaking in large systems, we simulate the wave packet dynamics of electrons in the hydrogenated diamond nanoparticle $C_{197}H_{112}$. We find that surface core ionizations cause emission of carbon fragments and protons through a direct Auger mechanism, whereas deeper core ionizations cause hydrides to be emitted from the surface via remote heating, consistent with results from photon-stimulated desorption experiments [Hoffman A, Laikhtman A, (2006) *J Phys Condens Mater* 18:S1517–S1546]. This demonstrates that it is feasible to study the chemistry of highly excited large-scale systems using simulation and analysis tools comparable in simplicity to those used for classical molecular dynamics.

electron force field | fermionic molecular dynamics | floating Gaussian orbitals

Great uncertainties remain concerning how highly excited states (~100 eV) induced by energetic photons, electrons, ions, or plasmas induce chemical processes at surfaces (1), particularly in large covalent systems (2) relevant to semiconductor fabrication (3). To determine the electron dynamics and atomic mechanisms involved in large-scale highly excited processes, we have developed the electron force field (eFF), a molecular dynamics model that includes electrons. We previously used eFF to compute the thermodynamic properties of warm dense hydrogen, and found excellent agreement with high-level theory, as well as both static compression and dynamic shock experiments (4).

We report now the application of eFF to study Auger processes in a hydrogenated diamond nanoparticle $C_{197}H_{112}$ (Fig. 1*A*). In the Auger process, ionization of a core electron leads to the collapse of a valence electron into the core hole, together with the ejection of another valence electron, all over several femtoseconds (5). During and after this time, secondary processes occur, causing protons, hydrides, and other species to desorb from hydrogen-terminated surfaces (1). We study the coupled electron-nuclear dynamics of both the primary Auger and accompanying secondary processes, ionizing core electrons both at the diamondoid surface and at different depths below the surface. In this way, we determine how the distance over which an Auger excitation relaxes and propagates affects the energies of electrons and composition of atomic species desorbed from the surface.

In eFF, all electrons, valence and core, are modeled as spherical Gaussian wave packets:

$$\Psi(\mathbf{r}) \propto \prod_i \exp\left[-\left(\frac{1}{s_i^2} - \frac{2p_{s,i}}{s_i}i\right)(\mathbf{r}-\mathbf{x_i})^2\right] \cdot \exp[i\mathbf{p_{x,i}}\cdot\mathbf{r}],$$

while nuclei are modeled as classical charged particles moving in the mean field of the electrons. The positions $\mathbf{x_i}$ and sizes s_i of the electrons are continuously variable, giving them the flexibility to participate in covalent, ionic, multicenter, and even metallic bonding; $\mathbf{p_{x,i}}$ and $p_{s,i}$ are the corresponding conjugate momenta. This description is well-suited for representing highly excited systems, where electron density maxima and spreads may be distorted from equilibrium positions and values.

Substituting the above expression into the time-dependent Schrodinger equation and assuming a locally harmonic potential V leads to particularly simple equations of motion (6):

$$d\mathbf{p_x}/dt = -\nabla_x V,\ \mathbf{p_x} = m_{\text{elec}}\dot{\mathbf{x}}$$
$$dp_s/dt = -\partial V/\partial s,\ p_s = (3m_{\text{elec}}/4)\dot{s}$$

i.e., nuclei and electrons move classically, but with a "breathing" motion as electrons shrink and expand in size over time. We take m_{elec} to be an effective mass, as in the semiclassical theory of electron transport in semiconductors. In harmonic potentials, the effective mass reduces to the true electron mass, but in anharmonic potentials, particularly near singularities, m_{elec} may increase as the wave packet is distorted and slowed. In our simple model, we account for the possible variation of m_{elec} by performing simulations for multiple fixed m_{elec}.

The Hamiltonian includes electrostatics, a kinetic energy which is larger for smaller electrons, and a spin-dependent Pauli exclusion that acts between pairs of electrons (see *Materials and Methods* for the detailed energy expression). The Pauli potential is a function of the overlap between electrons, as well as their respective sizes, and contains three parameters set to reproduce the ground-state geometries of small molecules such as CH_4, C_2H_6, LiH, and B_2H_6. The parameters are the same for all electrons, and for all systems studied (4).

eFF may be viewed as an elaboration of fermionic molecular dynamics methods (7, 8), using a Pauli potential accurate enough that condensed systems with $Z > 1$ can be described; or as an approximate and time-dependent version of ab initio floating spherical Gaussian orbital (FSGO) theory (9), with exchange energy estimated as a pairwise sum.

Results

Ground states may be obtained from damped electron dynamics, or more efficiently by minimizing the overall energy with respect to the electron parameters. For diamond and hydrocarbons, the eFF Pauli potential causes the electrons to segregate naturally into core and valence shells, with electron density profiles similar to density functional theory (Fig. 1*B*). Potential energies of eFF electrons may be compared with the energies of Hartree–Fock (HF) Boys-localized orbitals: for the 1*s*, CH, and CC electrons of ethane, we have from eFF 237, 13.8, and 17.7 eV and from HF 305, 17.5, and 18.5 eV. Hence, CC electrons are properly bound, but CH and core electrons are underbound by ~20%, probably from the limited ability of single Gaussian functions to form cusps at nuclear centers (for H atom this leads to an error of 15%).

Fig. 2 shows for a $C_{196}H_{112}$ nanoparticle the dynamics of a core hole state evolving continuously into a two valence hole state. At time zero, a 1*s* electron with down spin is removed from the central carbon of the nanoparticle, which induces the down-spin electrons in the surrounding bonds to race inward to fill the hole. Of the four

Author contributions: J.T.S. and W.A.G. designed research; J.T.S. performed research; and J.T.S. and W.A.G. wrote the paper.

The authors declare no conflict of interest.

[1]To whom correspondence should be addressed. E-mail: wag@wag.caltech.edu.

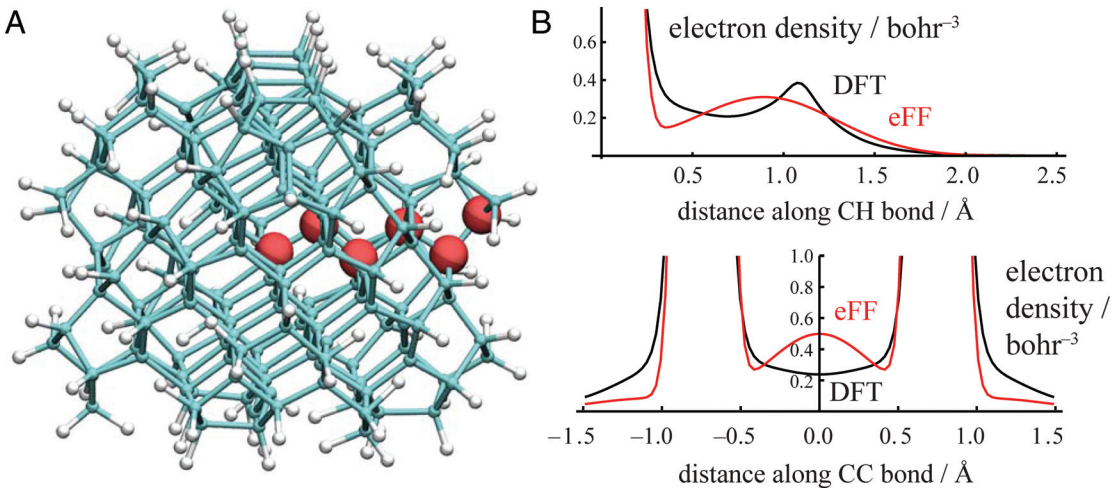

Fig. 1. The hydrogen-terminated diamond nanoparticle $C_{197}H_{112}$ used as a model system. (*A*) At the red sites, carbon core electrons are individually ionized and Auger dynamics are studied. (*B*) Comparison of electron densities between eFF and density functional theory (B3LYP/6-311g**) along a carbon–hydrogen bond in methane, and along a carbon–carbon bond in ethane.

electrons, only one (green) wins; the others bounce away from the now-filled core. One electron (red) feels the strongest repulsion, causing it to break free as an Auger electron, only to be trapped 20 fs later in the particle ~3 Å away, with its energy dissipated among the other electrons of the solid (not shown in the figure). The other two electrons (blue and purple) stay in bonds to the same nucleus, but remain highly excited, even after 50 fs.

In these dynamics we set $m_{elec} = m_{p(roton)}$, which leads to a core hole lifetime $\tau = 3.8 \pm 0.9$ fs for CH_4 (300 K, 500 trajectories), comparable to the experimental value $\tau_{expt} = 7.9 \pm 1.0$ fs (10), based on linewidth. Using $m_{elec} = m_p/1,836$ (mass of an electron) leads to $\tau = 0.09 \pm 0.02$ fs, smaller by nearly $1/\sqrt{1,836}$. Aside from an overall time-scaling, changing m_{elec} does not change the basic events observed: core hole filling, ejection of a secondary electron, and excitation of neighboring electrons.

When electrons escape the nanoparticle, their size increases linearly with time, as expected from a free particle wave packet, and we consider them to be ionized when their size exceeds 5 bohr. Fig. 3*A* shows the energy distribution of ejected electrons, obtained from 990 trajectories initiated by ionizing each of the six sites shown in Fig. 1. Nearly all of the ejected electrons (95–98%), both fast and slow, originate from the valence shell of the core ionized atom. Here using $m_{elec} = m_p$ (which leads to a reasonable core hole lifetime) leads to excessive dissipation, suppressing the emission of fast Auger electrons. But using $m_{elec} = m_p/1,836$ leads to a proper fast Auger peak for core excitation of atoms within three layers of the diamondoid surface.

The eFF Auger peak appears at a too-low energy, 95 eV [(eFF, outer surface) versus 263 eV (experiment, diamond surface (11))], due primarily to the reduced IP of the C(1*s*) electrons in eFF, which leaves less energy available for the Auger process. In addition, some of the energy is trapped in a core exciton (60–80 eV). Even so, the key features of the energy spectrum are correct. For example, in addition to the Auger peak, we find emission of low-energy electrons (0–10 eV) that appear to be the excited but non-Auger electrons of Fig. 2; similar energy distributions (4–8 eV) have been observed experimentally (12).

A hallmark of Auger spectroscopy is its surface selectivity, which exists because secondary electrons emitted >5 Å below the surface are trapped and not detected (13). Indeed we observe no fast Auger peak when diamondoid carbons >3 Å below the surface are ionized (our diamondoid has a radius of 6.5 Å). We find that trapped Auger electrons dissipate their energy away to surrounding bulk electrons over tens of femtoseconds.

Fig. 3*B* shows the atomic composition of fragments emitted from the nanoparticle after Auger excitation at different sites (using $m_{elec} = m_p$). An outer layer excitation produces hydrogen and carbon fragments with yields of 0.67 C, 0.17 CH, and 0.02 CH_2 per core ionization. Subsurface excitations, however, release only one species, the hydride ion H^-. This remote bond breaking is a strange phenomenon, and to understand why it occurs for H^-,

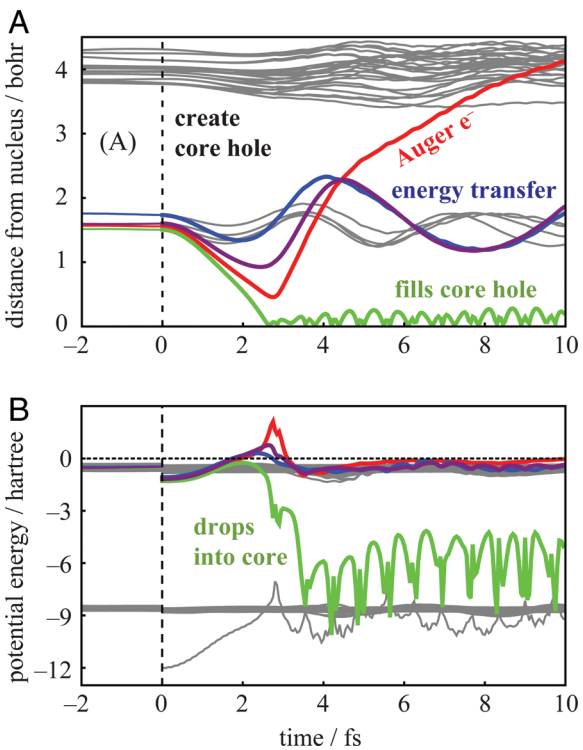

Fig. 2. Single Auger trajectory after ionization of a carbon core electron at the center of the diamond nanoparticle ($m_{elec} = m_p$). Valence electrons surrounding the core hole with the same spin as the ionized core electron are highlighted in red, green, blue, and purple. (*A*) Distance of valence electrons from the core hole, showing the green electron filling the core hole, the red electron being ejected (and trapped after 20 fs, not shown), and the blue and purple electrons being excited. (*B*) Potential energy of valence and core electrons, showing the conversion of the green electron from a valence to a core electron.

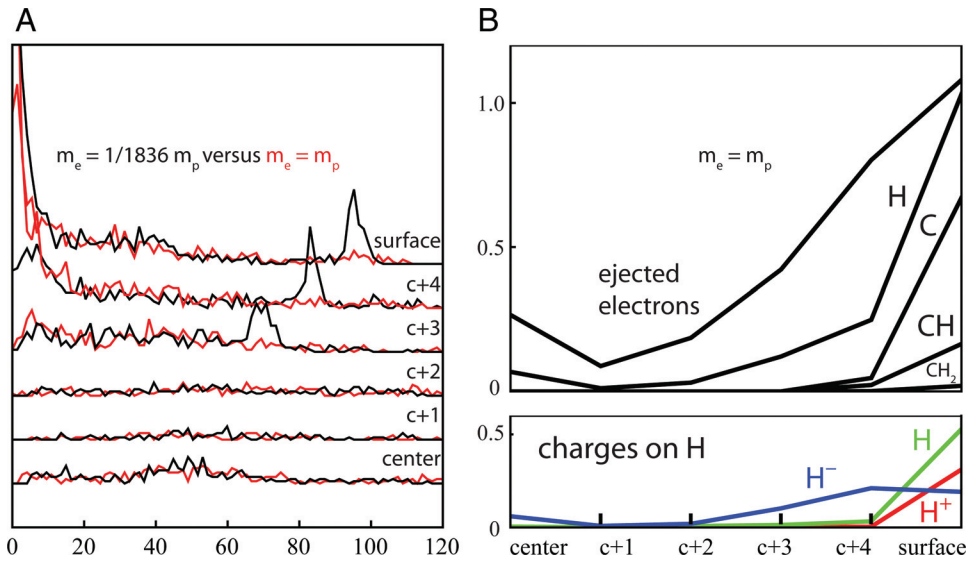

Fig. 3. Ejected electron and atomic fragment statistics from the nanoparticle. Aggregated over 5,940 independent Auger trajectories of the nanoparticle, from 990 snapshots at 300 K and the six different Auger sites shown in Fig. 1. The equilibration was performed over 1.0 ps (Δt = 5 as), with snapshots extracted over the last 0.5 ps; from the snapshots, a carbon 1*s* electron was instantaneously removed, and Auger dynamics was propagated for 50 fs (Δt = 1 as). (*A*) Histogram of ejected electron kinetic energies (radial + translational motions), where an electron is considered ionized if its size is >5 bohr after 50 fs. (*B*) Atomic composition of fragments separated from the nanoparticle after 50 fs, where the thresholds for a bond to be considered broken are as follows: d_{CC} > 2.5 Å, d_{CH} > 1.8 Å, d_{HH} > 1.5 Å. Charges associated with the desorbed hydrogens are analyzed in more depth by using the procedure outlined in Fig. 4.

but not for H and H^+, we examined the detailed electron motions of the Auger process in adamantane ($C_{10}H_{16}$). This small molecule is convenient to study, because a relatively large number of CH bonds is exposed to each core ionization.

Fig. 4 shows the fragmentation over time of CH bonds in core-ionized adamantane, tracking the lengths of the bonds and the charges associated with the protons. This analysis, performed over 410 trajectories, can be compared with a recent experiment (14), where a hydrogenated diamond surface was exposed to photons with energies near the core level, causing protons and hydride ions to be desorbed (the detector was insensitive to neutral species). The proton ion signal was predominantly a step function relative to the incident electron energy, suggesting that protons were emitted via a direct Auger mechanism. However, the hydride ion signal had a complex dependence with incident photon energy that correlated well with the secondary electron signal, suggesting that hydrides were released via an indirect mechanism involving secondary electrons as an intermediary.

Our simulations find that most hydrogens ejected (61%) from adamantane were attached to the Auger-excited atom (see Fig. 4*A*). In this *direct Auger* pathway, the majority of the hydrogens are emitted as protons (63%) or hydrogen atoms (34%), consistent with experiment.

The other emitted hydrogens originated from non-Auger excited atoms. Most of these (32%) result from thermal motion of the electrons; the electrons remain bound to the separating nuclei at all times, and no external electrons approach the nuclei (see Fig. 4*B*). We denote this the *indirect thermal* pathway, and find that the hydrogens are emitted mostly as hydrides (76%), consistent with experiment.

However, we also find that a small percentage (7%) of hydrogens ejected from non-Auger atoms come from a *secondary impact* pathway (see Fig. 4*C*). In this pathway, an excited valence electron

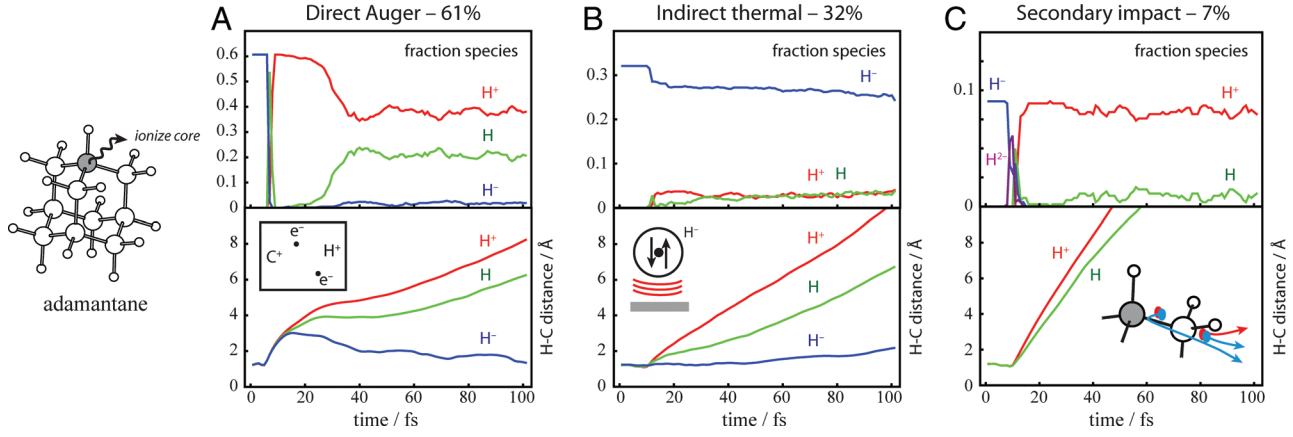

Fig. 4. Hydrogen desorption mechanisms obtained from trajectories of core-ionized adamantane ($C_{10}H_{16}$). (*Upper figures*) Distribution of charges associated with the ejected protons, computed assuming that an electron is bound to a proton if it satisfies $E_{nuc-elec} = -\mathrm{Erf}(\sqrt{2}R/s)/R < -0.6$ hartree, where R is the nuclear-electron distance and s is the electron size (bohr). (*Lower figures*) Carbon-hydrogen distance over time. The populations are separated into H^+/H/H^- categories based on the instantaneous charge present at t = 100 fs; 410 trajectories were considered (300 K), over which 676 hydrogens were ejected. (*A*) Direct Auger products. (*B*) Indirect thermalized products. (*C*) Products from secondary impact.

from the Auger process smashes into a carbon–hydrogen bond, causing the charge around the proton to increase momentarily (shown as H^{2-} in Fig. 4), along with the bond to fragment, with a proton scattered in one direction (88% of cases), along with two electrons in other directions. Because line-of-sight targeting is required, only hydrogens one bond separated from the Auger site depart via this mechanism.

Experimentally, it has been observed that protons produced via photon-stimulated desorption (PSD) on hydrogenated diamond are emitted with a doubly peaked kinetic energy distribution (14). We interpret these two classes of protons as originating from direct Auger versus secondary impact pathways, with direct Auger protons ejected more slowly because of the presence of electrons that linger in the bond over the core hole lifetime.

Discussion

The simple eFF model captures basic features of the Auger process, and explains how Auger excitations at different sites in a nanoparticle induce electrons of different energies and fragments of different compositions to be emitted from the surface. eFF accounts for the role of energy propagation within the bulk solid, and for the detailed motions of electrons in the surface bonds. Relevant mechanisms are extracted directly from electron dynamics trajectories, using analyses similar to those performed on classical molecular dynamics (nuclear) trajectories.

We can compare the mechanisms we observed by eFF with existing rationalizations of electron- and photon-stimulated desorption. Proton emission has been explained in terms of a Knotek–Feibelman model (15, 16), where after core hole ionization, one bonding electron fills the core hole, and the other is ejected; with no bonding electrons remaining, the bond breaks readily.

However, in the direct Auger pathway, we observe a limited disruption of the electron density in the bond to form a quasi-two-hole state, followed by recombination (after 30 fs) in one-third of the cases to form neutral but highly excited hydrogen atoms. The disruption occurs as the valence electrons fall toward the core hole, and can involve electrons that are highly excited but not ionized, as in postcollisional interactions (17).

For the desorption of negative ions such as hydrides, the indirect thermal pathway found by eFF involves a wide range of low-lying electron excitations that lead to desorption, since less energy is required to remove negative versus positive ions from a surface, as has been suggested previously (18).

Hence, we confirm that experimentally observed desorbed protons and hydrides result from different mechanisms, direct Auger versus indirect remote heating. We find that, in the direct Auger process, nonionized but excited electrons play a key role in causing carbon–hydrogen and carbon–carbon bonds to break. In addition, we discover with eFF a previously unknown minor pathway for proton desorption involving electron impact ionization, which may explain the doubly peaked kinetic energy distribution for ejected protons observed experimentally (14).

There does remain the question of whether it is proper to assume a range of effective dynamic electron masses, as we have done here. We note that many of the details of the Auger process, such as the gross electron motions and the energy distribution of slow electrons, do not appear to depend strongly on m_{elec}. The presence of the Auger peak does depend on m_{elec} but makes up at most 30% of the emitted electrons in all layers, and so the mechanisms described here should still be valid, with possible additional contributions from the traditional Knotek–Feibelman pathway.

Overall, we have demonstrated that eFF may be applied to study electron dynamics in large systems. More specifically, eFF should provide a useful tool for understanding interactions of excited states of matter with surfaces, and for optimizing electron etching processes for microelectronics applications.

Materials and methods

Full Hamiltonian for the Electron Force Field. The overall energy is a sum of the Hartree product kinetic energy, Hartree product electrostatic energy, and a pairwise sum that approximates the effect of the Pauli principle (antisymmetrization):

$$E = E_{\mathrm{ke}} + E_{\mathrm{nuc\cdot nuc}} + E_{\mathrm{nuc\cdot elec}} + E_{\mathrm{elec\cdot elec}} + E_{\mathrm{Pauli}}$$

which can be broken down further as follows, where s_i are the electron sizes, x_{ij} are the interelectron distances, and R_{ij} are the nuclear-nuclear and nuclear-electron distances:

$$E_{\mathrm{ke}} = \sum_i \frac{3}{2}\frac{1}{s_i^2}$$

$$E_{\mathrm{nuc\cdot nuc}} = \sum_{i<j} \frac{Z_i Z_j}{R_{ij}}$$

$$E_{\mathrm{nuc\cdot elec}} = -\sum_{i,j} \frac{Z_i}{R_{ij}} \mathrm{Erf}\left(\frac{\sqrt{2}R_{ij}}{s_i}\right)$$

$$E_{\mathrm{elec\cdot elec}} = \sum_{i<j} \frac{1}{x_{ij}} \mathrm{Erf}\left(\frac{\sqrt{2}x_{ij}}{\sqrt{s_i^2+s_j^2}}\right)$$

$$E_{\mathrm{Pauli}} = \sum_{\sigma_i=\sigma_j} E(\uparrow\uparrow)_{ij} + \sum_{\sigma_i\neq\sigma_j} E(\uparrow\downarrow)_{ij}$$

where $E(\uparrow\uparrow)$ and $E(\uparrow\downarrow)$ are the Pauli potential functions:

$$E(\uparrow\uparrow)_{ij} = \left(\frac{S_{ij}^2}{1-S_{ij}^2} + (1-\rho)\frac{S_{ij}^2}{1+S_{ij}^2}\right)\Delta T_{ij}$$

$$E(\uparrow\downarrow)_{ij} = \frac{\rho S_{ij}^2}{1+S_{ij}^2}\Delta T_{ij}$$

where ΔT is a measure of the kinetic energy change upon antisymmetrization, and S is the overlap between two wave packets:

$$\Delta T_{ij} = \frac{3}{2}\left(\frac{1}{\bar{s}_1^2}+\frac{1}{\bar{s}_2^2}\right) - \frac{2\left(3(\bar{s}_1^2+\bar{s}_2^2)-2\bar{x}_{12}^2\right)}{(\bar{s}_1^2+\bar{s}_2^2)^2}$$

$$S_{ij} = \left(\frac{2}{\bar{s}_i/\bar{s}_j+\bar{s}_j/\bar{s}_i}\right)^{3/2} \exp\left(-\bar{x}_{ij}^2/(\bar{s}_i^2+\bar{s}_j^2)\right)$$

where $\rho = -0.2$, $\bar{x}_{ij} = x_{ij}\cdot 1.125$, and $\bar{s}_i = s_i \cdot 0.9$.

Construction of the Diamondoid Nanoparticle. We created a $3\times3\times3$ supercell of bulk diamond in Chem3D 4.0 (CambridgeSoft and then), added hydrogens automatically, removed all of the methyl groups, and then reconstructed the (100) faces by hand. We optimized the resulting structure by using the MM2 force field in Chem3D. With a starting set of nuclear coordinates in hand, we placed electrons in starting positions by using the following rules: (*i*) core electron pairs are placed at the nuclear centers with size 0.333 bohr; (*ii*) carbon–carbon and carbon–hydrogen bonds are found by computing the pairwise distances between nuclei, and using the bond distance thresholds $d_{\mathrm{CH}} < 1.2$ Å and $d_{\mathrm{CC}} < 1.6$ Å; (*iii*) valence electrons are placed at the midpoints of carbon–carbon bonds with size 1.258 bohr, and at the position $\mathbf{r}_{\mathrm{CH}} = 0.293\mathbf{r}_{\mathrm{H}} + (1-0.293)\mathbf{r}_{\mathrm{C}}$ of carbon–hydrogen bonds with size 1.543 bohr. We then optimized using a conjugate-gradient algorithm the eFF Hamiltonian as a function of the nuclear and electron positions and electron sizes; at the end of the minimization the gradient was 2.9×10^{-5} hartrees/bohr.

Electron Density Along Bonds in Methane and Ethane. We optimized methane and ethane by using the procedure above, then computed eFF electron densities in two ways: (*i*) as a Hartree product wavefunction of eFF orbitals $\rho(\mathbf{r}) = \sum_i |\phi_i(\mathbf{r})|^2$, or (*ii*) as a Slater determinant of eFF orbitals $\rho(\mathbf{r}) = \sum_{ij}\phi_i(\mathbf{r})\phi_j(\mathbf{r})(\boldsymbol{S}^{-1})_{ij}$, where $\boldsymbol{S}$ is the overlap matrix of electrons. We plotted the electron density along the CH bond of methane, and along the CC bond of ethane. The densities computed from the Hartree product versus Slater determinant expressions differed by no more than 0.05 bohr^{-3} over the entire bond; in the manuscript, we plotted the Hartree product density. For comparison purposes, we also computed the electron densities by using B3LYP/6-311g** and HF/6-311g**, as implemented in Jaguar 7.0 (Schrodinger). The electron densities computed by using density functional theory versus Hartree–Fock theory did not differ appreciably.

Potential Energies of eFF Electrons in Ethane. We performed single-point eFF calculations on ethane, ethane missing a core electron, ethane missing a CH bonding electron, and ethane missing a CC bonding electron. Electrons were removed without changing the positions or sizes of any other electrons, and the nuclear positions were kept fixed. We then computed the potential

energy as a difference between the energies of these frozen wavefunctions, i.e., ethane and ionized ethane. For comparison purposes, we used HF/6-311g** in Jaguar 7.0 to optimize the geometry of ethane, performed a Boys localization of the core and valence orbitals, and printed out the energies of the localized orbitals.

Dynamics of the Auger Process. We performed eFF dynamics by using a velocity Verlet algorithm. Individual trajectories were integrated in the NVE (microcanonical) ensemble. We equilibrated the diamond nanoparticle at 300 K by starting with an energy-minimized geometry, giving the nuclei a Maxwell–Boltzmann distribution of initial velocities, and integrating an NVE trajectory over 1.0 ps (time step, 5 as) with $m_{\text{elec}} = m_{\text{p}}$. By varying the temperature of the initial velocity distribution (~600 K), we obtained a correct final temperature with energy properly partitioned between all degrees of freedom. We computed the temperature by using the virial expression $\frac{3}{2}k_{\text{B}}T = \frac{1}{N_{\text{nuc}}} \times \langle \sum_i \frac{1}{2} m_i v_i^2 \rangle$, where i is taken over all nuclear and electronic degrees of freedom.

We then extracted snapshots of the equilibrium trajectory over the last 0.5 ps; we took 990 snapshots at regular intervals. From these snapshots, we removed carbon 1*s* electrons from the sites shown in Fig. 1. Thus, we generated $990 \times 6 = 5,940$ independent starting core-ionized geometries. We performed dynamics from those geometries over 50 fs (time step, 1 as) for $m_{\text{elec}} = m_{\text{p}}$, and over $50 \times 1,836^{-1/2}$ fs (time step, $1 \times 1,836^{-1/2}$ as) for $m_{\text{elec}} = m_{\text{p}}/1,836$.

For Fig. 2*A*, we plotted the positions of the valence electrons relative to the core hole over the course of a single Auger trajectory (with the center ionized). We took valence electrons to be any electrons with size >0.5 bohr at time zero. To create a trajectory for points before time zero, we inverted the nuclear and electron velocities of the non-core-ionized starting geometry and computed dynamics backward with a 5-as time step. For Fig. 2*B*, we computed the potential energies for each electron over the course of the trajectory by summing over all the eFF energy terms that included interactions with that electron.

Histogram of Ejected Electron Energies. To compute the kinetic energies of ejected electrons, we took electrons with size >5 bohr after 50 fs, then calculated the quantity $\text{KE} = \frac{1}{2} m_{\text{elec}}(v_x^2 + v_y^2 + v_z^2) + \frac{1}{2} \cdot \frac{3}{4} m_{\text{elec}} v_s^2$. The position or momentum of a single electron is not strictly speaking well-defined, as they are indistinguishable particles, but in the case that an electron is well-separated in phase space from other electrons, it can be effectively "factored out" of the wavefunction.

Atomic Composition of Ejected Atomic Fragments. We divide a given configuration of nuclei into molecular fragments by using the following algorithm: (*i*) two atoms are connected if the distance between them falls below a threshold distance: $d_{\text{CC}} > 2.5$ Å, $d_{\text{CH}} > 1.8$ Å, $d_{\text{HH}} > 1.5$ Å; (*ii*) use an equivalence class analysis to distinguish disconnected classes from each other; (*iii*) determine the elemental composition of each group of atoms. We then count the number of different fragment types at the end of each trajectory.

Charges on Ejected Hydrogen Species. We found hydrogen fragments by using the procedure above, and computed the number of electrons associated with the proton at 50 fs by using a potential energy threshold: $E_{\text{nuc-elec}} = -\frac{1}{R}\text{Erf}\left(\frac{\sqrt{2}R}{s}\right) < -0.6$ hartrees, where R is the nuclear-electron distance and s is the electron size. For each proton, we scanned over all electrons in the system, eliminating ones too large or too far away with a rough threshold, then applying the above potential energy criterion to find electrons associated with the proton. The optimum energy threshold was selected by plotting histograms of electron–nuclei potential energies, and finding a value that clearly demarcated the proton–electron interaction peak.

Charges Associated with the Carbon–Hydrogen Bond Protons. We generated a distribution of adamantane geometries at 300 K, and performed dynamics on core-ionized snapshots by using the procedure above. We then computed the charge associated with the CH bond proton by using the procedure outlined above.

Carbon–Hydrogen Bond Distances over Time. We separated the adamantane Auger trajectories into $H^+/H/H^-$ categories based on the instantaneous charge on the CH bond proton present at 100 fs. We then averaged the CH bond distance over all the trajectories in each category.

ACKNOWLEDGMENTS. We thank H. P. Gillis for helpful discussions. This work was supported by the United States Department of Energy (Advanced Simulation and Computing) and the Defense Advanced Research Projects Agency/Office of Naval Research (Predicting Real Optimized Materials). We used computing facilities at Los Alamos National Labs to perform the dynamics calculations.

1. Ramsier RD, Yates JT (1991) Electron-stimulated desorption: principles and applications. *Surf Sci Rep* 12:243–378.
2. Ramaker DE (1982) Covalent interaction effects in electron/photon-stimulated desorption. *J Vac Sci Tech A* 1(2):1137–1144.
3. Gillis HP, *et al.* (1995) Low-energy electron-enhanced etching of Si(100) in hydrogen helium direct-current plasma. *Appl Phys Lett* 66(19):2475.
4. Su JT, Goddard WA III (2007) Excited electron dynamics modelling of warm dense matter. *Phys Rev Lett* 99:185003.
5. Thompson M, Baker MD, Christie A, Tyson JF (1985) *Auger Electron Spectroscopy* (Wiley, New York).
6. Heller EJ (1975) Time-dependent approach to semiclassical dynamics. *J Chem Phys* 62:1544–1555.
7. Feldmeier H, Schnack J (2000) Molecular dynamics for fermions. *Rev Mod Phys* 72:655–688.
8. Jakob B, Reinhard P-G, Toepffer C, Zwicknagel G (2007) Wave packet simulation of dense hydrogen. *Phys Rev E* 76:036406.
9. Frost AA (1967) Floating spherical Gaussian orbital model of molecular structure. I. Computational procedure. LiH as an example. *J Chem Phys* 47:3707–3713.
10. Köppe HM, *et al.* (1996) High-resolution C 1*s* photoelectron spectra of methane. *Phys Rev A* 53:4120–4126.
11. Krainsky IL, Asnin VM, Petukhov AG, Foygel M (1997) Auger spectroscopy of hydrogenated diamond surfaces. *Phys Rev B* 56:13529–13534.
12. Asnin VM, Krainsky IL (1998) Fine structure in the secondary electron smission peak for diamond crystal with (100) negative electron affinity surface. *Appl Phys Lett* 73:3727.
13. Zemek J, Potmesil J, Vanecek M, Lesiak B, Jablonski (2005) A Inelastic mean-free path of electrons at nanocrystalline diamond surfaces. *Appl Phys Lett* 87:262114.
14. Hoffman A, Laikhtman A (2006) Photon stimulated desorption of hydrogen from diamond surfaces via core-level excitations: fundamental processes and applications to surface studies. *J Phys Condens Matter* 18:S1517–S1546.
15. Knotek ML, Feibelman PJ (1978) Ion desorption by core-hole Auger decay. *Phys Rev Lett* 40:964–967.
16. Jennison DR, Kelber JA, Rye RR (1982) Localized Auger final states in covalent systems. *Phys Rev B* 25:1384–1387.
17. Kuchiev MU, Sheinerman SA (1989) Post-collisional interaction in atomic processes. *Sov Phys Usp* 32:569–587.
18. Knotek ML (1984) Stimulated desorption. *Rep Prog Phys* 47:1499–1561.